Hydroxyl transport mechanisms upon passivation of Cr-Fe-Co-Ni-Mo multi-principal element alloy surfaces investigated by isotopic labelling

Xueying Wang, Dimitri Mercier, Sandrine Zanna, Antoine Seyeux, Loïc Perrière, Mathilde Laurent-Brocq, Ivan Guillot, Vincent Maurice, Philippe Marcus

Author preprint published in Applied Surface Science
https://doi.org/10.1016/j.apsusc.2024.159558

Hydroxyl transport mechanisms upon passivation of Cr-Fe-Co-Ni-Mo multi-principal element alloy surfaces investigated by isotopic labelling

Xueying WANG[1], Dimitri MERCIER[1*], Sandrine ZANNA[1], Antoine SEYEUX[1], Loïc PERRIERE[2], Mathilde LAURENT-BROCQ[2], Ivan GUILLOT[2], Vincent MAURICE[1], Philippe MARCUS[1*]

[1] *PSL Research University, CNRS - Chimie ParisTech, Institut de Recherche de Chimie Paris, Physical Chemistry of Surfaces Group, 11 rue Pierre et Marie Curie, 75005 Paris, France*

2 Université Paris Est Creteil, CNRS, ICMPE, UMR7182, Thiais F-94320, France

**Corresponding authors: D. Mercier (dimitri.mercier@chimieparistech.psl.eu), P. Marcus (philippe.marcus@chimieparistech.psl.eu).*

Abstract

Time-of-flight secondary ion mass spectrometry (ToF-SIMS) combined with deuterium labelling (D_2O), and X-ray photoelectron spectroscopy (XPS) were applied to investigate the interfacial transport mechanisms of hydroxyls between aqueous electrolyte and outer part of the protective oxide film during passivation of $Cr_{15}Fe_{10}Co_5Ni_{60}Mo_{10}$ multi-principal element alloy surfaces. A ToF-SIMS signal treatment methodology was developed to retrieve the in-depth distribution of deuterated hydroxides in the nanometer-thick surface oxide film. After immersion at free potential or anodic passivation in acidified D_2O, the initial bilayer structure is retained. The use of heavy water electrolyte has no effect on the composition alterations induced by passivation. Deuterated species were detected mostly in the outer layer of the surface oxide film. Pure inward hydroxyl diffusion from electrolyte/oxide to oxide/metal interface is excluded from being primarily responsible for oxide film growth induced by anodic passivation. The hydroxyls from the dissolving hydroxide species are retained in the oxide film and participate in forming Cr hydroxide, thus reducing the hydroxyl surface uptake from the electrolyte. This work provides deeper insight into the mechanisms of oxide growth and corrosion protection induced by anodic passivation.

Keywords: ToF-SIMS; Deuterium labelling; Corrosion protection; Passive oxide film; Hydroxyl transport mechanisms; Multi-principal element alloy

1 Introduction

Passivation is one of the most effective ways to protect alloys against corrosion. Passivation consists in the spontaneous formation of a self-repairing surface oxide film preventing the metallic substrate from being exposed to the environment. To be protective, the oxide film should be either thermodynamically stable or dissolving kinetically too slowly in the given conditions. Cr is one of the widely used passivating elements for endowing alloys with passivity. Its high oxygen affinity[1,2] ensures the spontaneous formation and self-repair of a Cr oxide layer; and the compactness and slow dissolution rate of Cr oxide [3,4] ensures the protection effect of the passive film. Thus, the passive state of Cr-containing alloys is a steady state in which oxide formation and dissolution occur simultaneously but very slowly, as described in various oxide growth models [5–10].

In view of the important role of passive oxide films in impeding corrosion processes, their composition, structure, and morphology have been intensively studied using techniques such as X-ray photoelectron spectroscopy (XPS) [11,12], time-of-flight secondary ion mass spectrometry (ToF-SIMS) [13,14], scanning tunneling microscopy (STM) [15–18], and transmission electron microscopy (TEM) [19,20]. Many works have revealed that protective oxide films formed on Cr-containing Fe- or Ni-based alloys are extremely thin with a thickness range of about 1-3nm and present an in-depth stratified structure[13,21–24] and lateral heterogeneities[2,25,26]. Generally, the inner part of the oxide film consists mainly of Cr oxide with a minor amount of other elements, and it is considered as the barrier layer endowing the covered

surface with high corrosion resistance[13,14,21,22,25]. The outer part of the oxide film can contain a mixture of oxides and hydroxides (Cr, Fe, Mo, Ni) depending on the substrate alloy composition[13,14,21,22,25]. Therefore, a simplified bilayer model with an inner layer enriched in Cr and an outer layer with diverse species is usually used for illustrating the oxide film formed on Fe- or Ni-based Cr-containing alloys[13,14,22,25]. The content of Cr and Mo species in the oxide film are always higher than their nominal content in the bulk alloy[12,21,25,27].

With the idea to design new alloys, multi-principal element alloys (MPEAs), forming a new class of alloys composed of several major elements instead of only one base element, have been developed over the last two decades[28,29]. The compositional flexibility endows MPEA systems with huge potential in property optimization, which triggered intensive research soon after their emergence. For designing highly corrosion-resistant MPEAs, CrFeCoNiMo is one of the prominent and most explored alloy systems[30–34]. Studies have proven the feasibility of producing single-phase *fcc* CrFeCoNiMo MPEAs with Mo content up to 15 at. % (*vs.* 2-2.5 at. % in 316L stainless steel), and have demonstrated the high corrosion resistance of such alloys[30–34]. Detailed surface analysis revealed that the surface oxide films formed on these MPEAs also present the typical stratified structure with Cr oxide concentrated in the inner part and other (hydr)oxides in the outer part[35,36]. Recently, XPS and ToF-SIMS measurements have suggested a combined effect of Mo and Cr for healing the Fe-rich weak sites of the barrier layer while density functional theory (DFT) simulation provided atomistic insight to explain the high corrosion resistance obtained with Cr,

Mo-containing MPEAs[35,37,38].

Since the protection provided by these passive oxide films involves dynamic equilibrium between oxide formation and oxide dissolution, one may interrogate the ion transport mechanisms within the film and across the passivated interface. Isotopic labelling is an effective approach for investigating elemental behavior during oxide film formation. ^{18}O is typically used for tracing the behavior of oxygen during oxidation [39–42]. Correspondingly, deuterium (D) can be used as isotopic marker for hydrogen or hydroxides. However, most hydrogen-related isotopic studies for alloys were launched in response to industrial demands concerning hydrogen embrittlement [43–45], focusing mainly on revealing the distribution of hydrogen atoms and their interactions with the bulk alloy microstructure[44,46–49]. In contrast, refined characterization of hydrogen and/or hydroxyl transport behavior between electrolyte and surface oxide film[47] for a fundamental understanding of the oxide film built-up process[43] is less emphasized. This relative lack of attention may be because hydroxides exist mainly in the outer part of passive films, while the high corrosion resistance is typically attributed to the inner barrier oxide layer [3,4]. Besides, the thinness of the oxide film, the difficulty in detecting hydrogen, and the residual hydrogen in ultra-high vacuum (UHV) analytical chambers[43] make such study difficult.

Being in direct contact with the external medium, the behavior of the outer oxide layer is essential for understanding the ion transport mechanisms across the passivated interface and must play a role in the penetration of aggressive species in the oxide film.

Several published works have already demonstrated the existence of deuterium/hydrogen in the oxide film [43,47,50] and an inward OH diffusion through oxide film in pressurized water reactors primary water, which is high-temperature high-pressure[43,50]. However, such studies are still missing for passivation mechanisms at room temperature, and the chemical environment of hydrogen atoms was not specified.

In this context, this work aims to investigate the ion transfer mechanisms between electrolyte and surface oxide film during dissolution and electrochemical passivation of single-phase *fcc* $Cr_{15}Fe_{10}Co_5Ni_{60}Mo_{10}$ (at.%) MPEA surfaces in sulfuric acid solution at room temperature. ToF-SIMS depth profiling using deuterium labelling for tracing hydroxyl, and XPS and ICP-OES analyses for monitoring cations were combined. Due to the similarity in mass of one deuterium atom D and two hydrogen atoms 2H, signals representing deuterated hydroxides are seriously overlapped with 2H-containing signals representing non-deuterated hydroxides at the current resolution of 8000-10000 ($\frac{m}{\Delta m}$ for ^{28}Si) of ToF-SIMS analysis. Therefore, a methodology for extracting the deuterated hydroxide signals was developed and adopted in this work. This methodology is an improvement for isotopic study applied to nanometer-thick surface oxide films, enabling the investigations of diverse deuterated hydroxides. Based on the obtained results, the deuterium surface uptake during dissolution and passivation in D_2O is discussed, providing deeper insight into the cation and hydroxyl transport process across the oxide/electrolyte interface during electrochemical passivation at room temperature.

2 Experimental and methods

2.1 Sample preparation

Homogeneous single-phase *fcc* $Cr_{15}Fe_{10}Co_5Ni_{60}Mo_{10}$ (at.%) MPEA samples with a grain size of 61 ± 5 μm were studied in this work. The manufacturing of the alloy has been reported elsewhere[34]. The specimen surfaces were mechanically polished successively with 1200, 2400 and 4000 grade SiC paper, followed by diamond paste finish of 3, 1 and 0.25 μm. Samples were then ultrasonically cleaned for 5 min in acetone, ethanol and deionized water (Merk Millipore, resistivity of 18.2 MΩ.cm), and dried in compressed air flow.

The anodically passivated surfaces were prepared at room temperature with a 3-electrode cell comprising a saturated mercury sulfate reference electrode (MSE, $E_{SHE} = E_{MSE} + 0.64$ V), a Pt wire counter electrode and the MPEA sample surface constituting the working electrode. The working area was delimited to 1.13 cm² by a Viton O-ring. A VersaSTAT4 potentiostat (AMETEK) was used as controller. The electrolyte for passivation was 5 mL 0.05 M H_2SO_4 solution prepared from sulfuric acid (VMR, reagent ACS grade) and deionized water or D_2O (Eurisotop, deuterium purity of 99.97%). Anodic passivation was performed by stepping the potential to 0 V_{MSE} for 1 h after 15 min of stabilization at Open Circuit Potential (OCP). The surfaces passivated at OCP, hereafter referred to as immersed surfaces, were prepared in either 5 mL of pure water or 5 mL 0.05 M H_2SO_4 solution, one using deionized H_2O and the other one using D_2O. The duration of the immersions was 1 hour and 15 min, corresponding to the total time that the passivated surfaces were exposed to electrolyte. Prior to anodic passivation

or OCP immersion, the electrolytes were deaerated by bubbling Ar gas for 30 min to minimize dissolved oxygen. After immersion or passivation in sulfuric acid solution, the samples were rinsed with deionized water during several seconds and dried with compressed air. The samples were then introduced into XPS or ToF-SIMS UHV chamber for analysis. The air exposure duration during the transfer process was about 20 min.

2.2 Solution analysis

The sulfuric acid solution was analyzed before passivation (i.e., after 15 min of stabilization at OCP) and after passivation by ICP-OES to calculate the quantity of dissolved cations during passivation. The measurements were performed using an ICP-OES iCAP 6300 (Thermo Fisher Scientific) after passivation in 0.05 M H_2SO_4 prepared with H_2O. The solutions used for ICP-OES analysis were acidified with 5 wt.% HNO_3 solution. Calibration solutions from 0.03 ppm to 0.5 ppm were prepared for Cr, Fe, Co Ni and Mo with corresponding standard solution of 1000 µg/mL (Chem-Lab NV), 5 wt.% HNO_3 solution for acidification, and 0.05 M H_2SO_4 for ensuring the same matrix effect as the sample solutions. The quantity of dissolved cations was normalized to the working electrode area (1.13 cm^2).

2.3 Surface analysis

The stratified structure and composition of the surface oxide films after immersion at OCP or anodic passivation were determined by XPS and ToF-SIMS analysis.

XPS analysis was carried out in a Thermo Electron ESCALAB 250Xi spectrometer

with a pressure lower than 10^{-10} mbar in the analysis chamber. A monochromatic Al Kα X-ray source (hν = 1486.6 eV) was used. High-resolution spectra of the Cr 2p, Fe 2p, Co 2p, Ni 2p, Mo 3d, S 2p, O 1s, and C 1s core levels were recorded with a pass energy of 20 eV and a step size of 0.1 eV. The take-off angle of the photoelectrons was 90°. The fitting of the spectra was performed using Casa XPS software. The decomposition procedure and parameters were the same as previously established for the $Cr_{15}Fe_{10}Co_5Ni_{60}Mo_{10}$ MPEA, reported in details elsewhere [35,37,51]. In summary, Shirley type background was used and constraints on binding energy (BE), full width at half maximum (FWHM), lineshape, intensity ratio between spin–orbit doublets, and intensity ratio between photoelectron peak and Auger peak were applied for curve fitting. Reference lineshapes obtained on corresponding pure metals or pure Cr oxide were used to consider the asymmetry of metallic peaks and the multiplet splitting structure of Cr oxide peak. Other oxide or hydroxide peaks were fitted with symmetric Gaussian/Lorentzian product lineshape GL(x), where x defines the percentage of Lorentzian character. For the Cr 2p, Fe 2p, Co 2p, Mo 3d core level spectra, the entire region containing both $2p_{3/2}$ and $2p_{1/2}$ (or $3d_{5/2}$ and $3d_{3/2}$ for Mo 3d) peaks was decomposed due to the overlap between the spin–orbit doublets. For the Ni 2p spectra, only the Ni $2p_{3/2}$ region was decomposed since it is not overlapping with Ni $2p_{1/2}$ peaks.

ToF-SIMS depth profile elemental analysis was performed in an IONTOF ToF-SIMS 5 spectrometer with a pressure of 10^{-8} mbar or lower and operated in dual-beam operation mode. A 25 keV Bi^+ primary LMIG source delivering 1.2 pA target current over a 100 × 100 μm² area was used for static SIMS analysis. The static analysis was

interlaced with sputtering realized by a 0.5 keV Cs^+ sputter beam delivering 17 nA target current over a 300 × 300 μm² area. The two beams were at an incidence angle of 45° with respect to sample surface and well-aligned to ensure analysis from the center of the sputtered crater. The time acquisition interval of the data was 1.3 s. Negative ions were recorded because they are more sensitive to ion fragments coming from oxide matrices. For each surface, at least two depth profiles in two different zones were recorded to verify the uniformity of the surface. Data acquisition and processing were performed with the IONSPEC 7.2 software.

D^-, OD^- CrO_3D^-, NiO_2D^-, and $^{100}MoO_4D^-$ were selected as representative ion fragments for D, OD, and deuterated Cr, Ni, Mo hydroxides, respectively. However, the similarity in mass of one D (2.0141 amu) and two H (2.0157 amu) results in the overlap between the hydroxide signals containing one D (CrO_3D^-, NiO_2D^-, or $^{100}MoO_4D^-$) and the signals containing H_2 ($CrO_3H_2^-$, $NiO_2H_2^-$, or $^{100}MoO_4H_2^-$) at the mass resolution of 8000-10000 ($\frac{m}{\Delta m}$ for ^{28}Si). Therefore, based on the findings of changeless intensity ratios $\frac{MO_xH_2^-}{MO_xH^-}$ for M = Cr, Ni or ^{100}Mo for each kind of surface, and the consistency in nature between the deuterated or non-deuterated oxide films, equation (1) was used to extract the signal for deuterated hydroxides:

$$MO_xD^- = (MO_xH_2^-)_{raw} - MO_xH^- \times \left(\frac{MO_xH_2^-}{MO_xH^-}\right)_{reference} \quad (1)$$

Where:

- MO_xD^- is the characteristic signal for deuterated hydroxide calculated for the deuterated surface.
- $(MO_xH_2^-)_{raw}$ is the raw signal measured on the deuterated surface. It is in

fact the sum of deuterated hydroxide signal MO_xD^- and non-deuterated hydroxide signal $MO_xH_2^-$.

- MO_xH^- is the characteristic signal for non-deuterated hydroxide measured on the deuterated surface.
- $\left(\frac{MO_xH_2^-}{MO_xH^-}\right)_{reference}$ is the reference ratio obtained on the non-deuterated surface, prepared following the same procedure but in corresponding non-deuterated electrolyte.

In order to minimize the overlap with other signals, a specified mass interval was taken for each ion fragment instead of the whole peak detected in the mass spectrum. The mass intervals were maintained the same throughout this work in order to ensure the validity of the reference ratios.

Due to the existence of multiple laboratory-scale stable Mo isotopes of important relative abundance (9.2 % ^{94}Mo, 15.9 % ^{95}Mo, 16.7 % ^{96}Mo, 9.6 % ^{97}Mo, 24.3 % ^{98}Mo, 9.7 % ^{100}Mo), there were overlaps between hydroxylated fragments of lighter Mo isotope and non-hydroxylated Mo fragments of heavier Mo isotope, for example $^{98}MoO_4H_2^-$ and $^{100}MoO_4^-$. Therefore, ^{100}Mo, the heaviest stable Mo isotope, was selected instead of the principal isotope ^{98}Mo so that no overlap with heavier isotope could occur.

3 Results and Discussion

3.1 Deuterium detection in the oxide film

Two types of ToF-SIMS representative signals of interest were distinguished for

characterizing D-containing species in the oxide films covering the immersed and passivated $Cr_{15}Fe_{10}Co_5Ni_{60}Mo_{10}$ surfaces prepared in acidified D_2O. Figure 1 presents raw or treated ToF-SIMS negative ion depth profiles obtained on non-deuterated or deuterated passivated surfaces as an example for illustrating the detection of D-containing species in the surface oxide film.

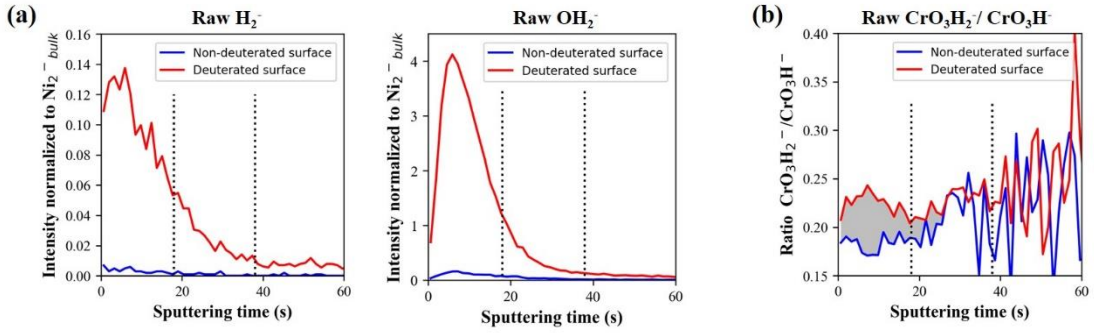

Figure 1 ToF-SIMS negative ion depth profiles of raw H^- and $^{18}OH^-$ signals (a), and of the raw intensity ratio $CrO_3H_2^-/CrO_3H^-$ (b) for anodically passivated $Cr_{15}Fe_{10}Co_5Ni_{60}Mo_{10}$ surfaces prepared in non-deuterated or deuterated solutions.

Figure 1(a) shows the depth profiles of the first type of characteristic signals, H_2^- [43,47,52] and OH_2^- [47]. The ordinate of the plots is the intensity of the signals normalized to the nickel signal in the alloy ($I/I_{Ni_{2\,(bulk)}^-}$). The abscissa is the sputtering time, reflecting the depth from the surface. The dashed lines mark the positions of the outer/inner oxide layer interface (at around 18 s) and oxide/alloy interface (at around 38s). The definitions of the interfaces are explained in section 3.2. Since D and 2H are not distinguishable at the present mass resolution, the measured raw H_2^- and OH_2^- signals were in fact (H_2^-+D^-) and (OH_2^-+OD^-), respectively. However, as shown in Figure 1(a), the intensities of raw (H_2^-+D^-) and (OH_2^-+OD^-) signals recorded on the deuterated surface were much higher than those recorded on the non-deuterated surface. This significant difference in intensity suggests that there was deuterium originating

from the electrolyte in the oxide film after passivation, and that in practice the H_2^- and OH_2^- contributions to the signals are negligible compared to D^- and OD^-. Therefore, the recorded raw (H_2^-+D^-) and (OH_2^-+OD^-) signals were used directly as characteristic ions for reconstructing the distributions of D and OD hereafter.

The second type of characteristic ions consists of CrO_3D^-, FeO_2D^-, NiO_2D^-, and $^{100}MoO_3D^-$, representing deuterated hydroxides of Cr, Fe, Ni, and Mo, respectively. These signals also overlap with corresponding 2H-containing signals $MO_xH_2^-$ in the mass spectra. These $MO_xH_2^-$ signals, characterizing the non-deuterated hydroxides, are not negligible according to their intensity measured on non-deuterated surfaces. However, it was observed that the intensity ratio $\frac{\text{raw } CrO_3H_2^-}{\text{raw } CrO_3H^-}$ for one surface is consistent and even insensitive to experimental conditions. Besides, the $\frac{\text{raw } CrO_3H_2^-}{\text{raw } CrO_3H^-}$ ratio obtained for deuterated surfaces is always higher than that for corresponding non-deuterated surfaces in the superficial region where hydroxides existed. The extra part should result from deuterated species. Figure 1(b) presents the depth profile of the $\frac{\text{raw } CrO_3H_2^-}{\text{raw } CrO_3H^-}$ ratio for the deuterated passivated surface as an example. The difference between the two curves, marked with gray shadowing, must be related to the CrO_3D^- contribution to the signal which indicates the existence of deuterated Cr hydroxide. At deeper location in the oxide inner layer and bulk alloy regions, the fluctuating signals resulted only from background noise enlarged by the division operation and are not characteristic of the species distribution. Similar higher $\frac{\text{raw } MO_xH_2^-}{\text{raw } MO_xH^-}$ ratio in the superficial region on deuterated surface was also observed for Fe, Ni and Mo.

Figure 1 proves with the D^- and OD^- signals that there is a certain quantity of

deuterium in the surface oxide film after passivation in deuterated electrolyte. It also elucidates with raw intensity ratios a potential way to characterize specific deuterium species by ToF-SIMS. However, since isotope distribution should tend towards equilibrium, it cannot be concluded whether the deuterium surface uptake was principally due to passivation or to isotopic exchange[53]. Therefore, the same analyses on $Cr_{15}Fe_{10}Co_5Ni_{60}Mo_{10}$ surfaces immersed in pure D_2O or 0.05 M H_2SO_4 prepared with D_2O are necessary to differentiate the effects of passivation from other parasitic processes. For the surfaces immersed in pure or acidified D_2O, direct usability of raw (H_2^-+D^-) and (OH_2^-+OD^-) signals for representing D and OD and the higher $\frac{\text{raw } MO_xH_2^-}{\text{raw } MO_xH^-}$ (M=Cr, Ni or ^{100}Mo) ratio in the presence of deuterium were also observed.

3.2 The structure and composition of the oxide films

The prerequisite to using the $\frac{MO_xH_2^-}{MO_xH^-}$ ratio obtained on non-deuterated surfaces as a reference for extracting D-containing signals for deuterated surfaces is to verify that the $\frac{MO_xH_2^-}{MO_xH^-}$ ratio obtained on non-deuterated surfaces is still valid for the corresponding species on deuterated surfaces. The validation relied on examining the consistency of the oxide film nature in the absence and presence of deuterium. The structure and the composition of non-deuterated oxide films and corresponding deuterated oxide films were investigated and compared to examine whether the reactivity difference between D and H [54] leads to modifications on the oxide film except for the substitution of H by D.

The composition of the oxide film was determined by XPS analysis using the fitting method described previously[35]. Figure 2 shows the XPS high-resolution spectra of

the Cr 2p, Ni $2p_{3/2}$, Fe 2p, Mo 3d, and Co 2p core level regions recorded on non-deuterated or deuterated passivated surfaces as an example for illustrating the consistency of identified species.

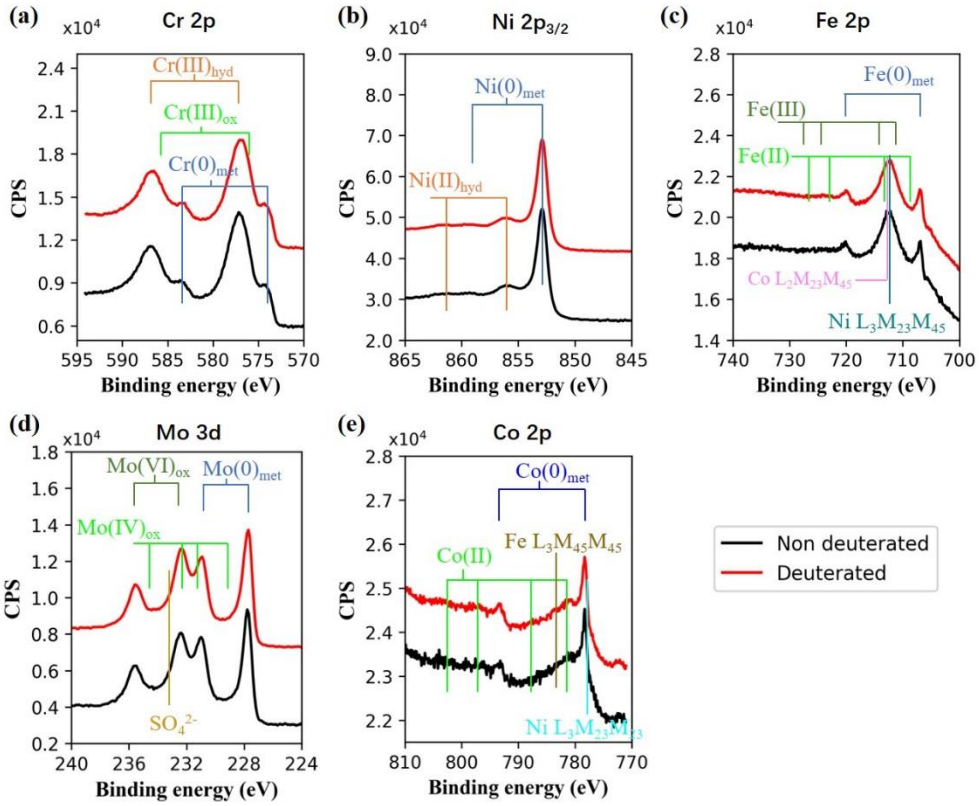

Figure 2 XPS Cr 2p (a), Ni $2p_{3/2}$ (b), Fe 2p (c), Mo 3d (d) and Co 2p (e) core level spectra for $Cr_{15}Fe_{10}Co_5Ni_{60}Mo_{10}$ surfaces anodically passivated in 0.05 M H_2SO_4 solution prepared with H_2O or D_2O.

The decomposition of these XPS spectra identified the same species for both surfaces, namely Cr(III) oxide and hydroxide, Fe(II) and Fe(III) (hydr)oxides, Ni hydroxide, Mo(IV) and Mo(VI) (hydr)oxides. The same components were also identified for the $Cr_{15}Fe_{10}Co_5Ni_{60}Mo_{10}$ surfaces immersed in pure or acidified H_2O (D_2O).

Figure 3 displays the depth profiles illustrating the structure of the surface layers for surfaces immersed in pure H_2O (Figure 3(a)), pure D_2O (Figure 3(b)), acidified H_2O (Figure 3(c)), acidified D_2O (Figure 3(d)), or anodically passivated in acidified H_2O

(Figure 3(e)) or acidified D_2O (Figure 3(f)). The representative secondary ions determined in previous work for the $Cr_{15}Fe_{10}Co_5Ni_{60}Mo_{10}$ MPEA were used for reconstructing the depth profiles [35]. The H-free signals CrO^- (67.9354 amu), FeO_2^- (87.9248 amu), MoO_2^- (129.8952 amu), and MoO_3^- (145.8902 amu) represent Cr, Fe, Mo oxides, respectively. The Ni_2^- signal (115.8707 amu) represents metallic nickel. The $CrO_3H_x^-$ and $NiO_2H_y^-$ series of signals is typically used as characteristic ions for Cr hydroxide and Ni hydroxide in literature[13,14,35]. Here, $CrO_3H_2^-$ (101.9409 amu) and NiO_2H^- (88.9330 amu) are shown. The dashed lines indicate the inner/outer oxide layer interface and the oxide/metal interface, located using the convention of the position where the CrO^- and Ni_2^- signals reach 80% of their maximum intensity[35,37]. The profiles have been normalized by the intensity of Ni_2^- in the bulk alloy.

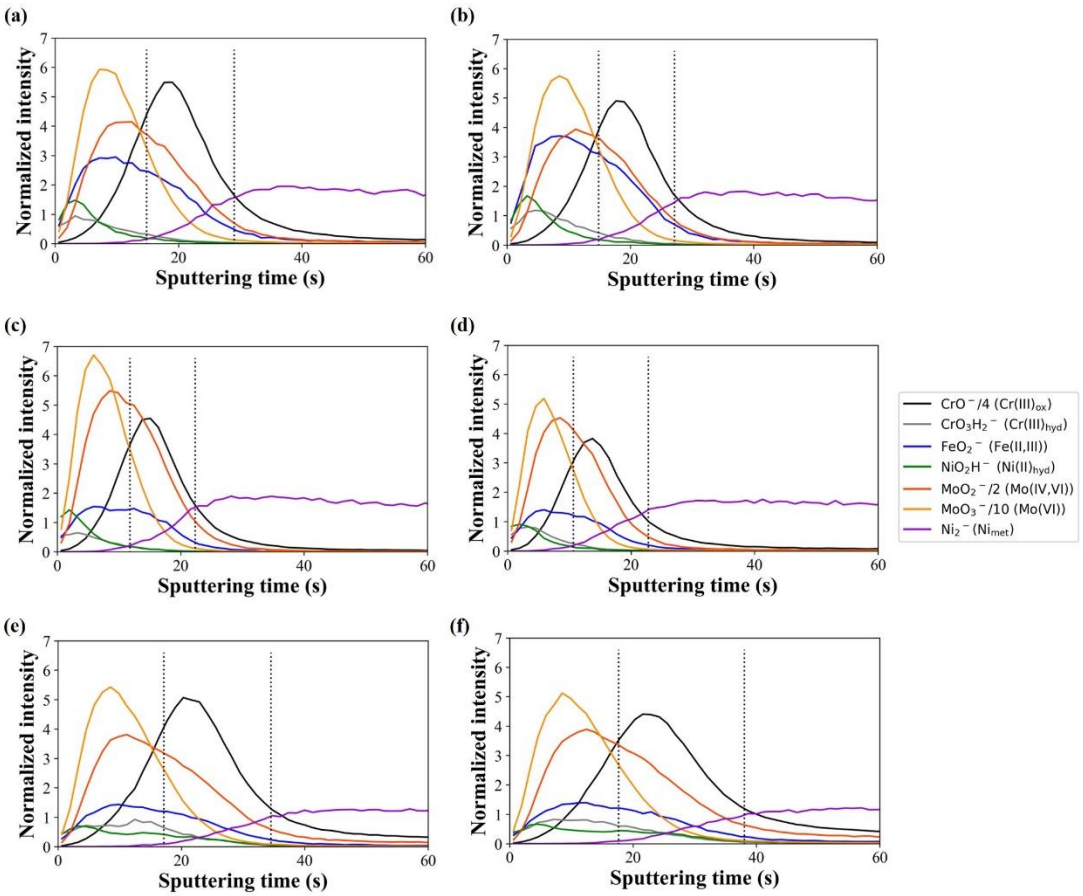

Figure 3 ToF-SIMS negative ion depth profiles for the $Cr_{15}Fe_{10}Co_5Ni_{60}Mo_{10}$ surfaces immersed at OCP in H_2O (a) or D_2O (b), immersed at OCP in 0.05 M H_2SO_4 prepared with H_2O (c) or D_2O (d), or anodically passivated in 0.05 M H_2SO_4 prepared with H_2O (e) or D_2O (f).

As shown in Figure 3(a)-(f), among the characteristic signals of (hydr)oxides, two distinct regions exist. $CrO_3H_2^-$, NiO_2H^-, FeO_2^-, MoO_2^-, and MoO_3^- signals always peak at sputtering times earlier than the CrO^- signal, showing that the hydroxide of Cr, Ni, and (hydr)oxides of Fe, Mo, are concentrated at a position more superficial than Cr oxide. As explained in previous work, the stratified distribution of these species is consistent with a bilayer structure of the oxide film. The inner layer of the oxide film is enriched in Cr oxide, and the outer layer is composed of Cr, Fe, Mo oxides or hydroxides.

For each of the three pairs of surfaces, no significant modification on the stratified structure of the oxide film was observed between non-deuterated (Figure 3a, c, e) or deuterated (Figure 3b, d, f) state, indicating that the deuteration of the electrolyte did not lead to structural modifications of the surface oxide film.

Based on the bilayer model, quantification was then carried out using XPS intensities and the intensity attenuation equations for an electron flux passing through surface layers [22,55]. The values of photoionization cross-section of each element for Al Kα emission at 1486.6 eV and the inelastic mean free paths of the emitted photoelectrons were taken from J. H. Scofield [56] and S. Tanuma *et al*. [57], respectively. The alloy density is 8.3 $g.cm^{-3}$ and an assumed oxide film density of 4.5 $g.cm^{-3}$ was used. The XPS intensity of Cr(III) oxide component was attributed to the inner layer and the intensities of the other species to the outer layer[35]. The calculated

composition of the outer oxide layer and thickness of the inner and the outer layers are compiled in Table 1.

	Cationic constitution of the outer layer					Thickness (±0.1 nm)	
	Cr (±2 at%)	Fe (±3 at%)	Co (±3 at%)	Ni (±2 at%)	Mo (±2 at%)	Outer layer	Inner layer
Native oxide film[35]	17	13	3	46	21	1.3	0.2
Immersion in H_2O	43	10	2	22	23	1.5	0.2
Immersion in D_2O	41	11	2	24	22	1.5	0.3
Immersion in 0.05 M H_2SO_4 (H_2O)	32	8	2	29	29	1.3	0.2
Immersion in 0.05 M H_2SO_4 (D_2O)	29	8	3	30	30	1.3	0.2
Passivation in H_2O with 0.05 M H_2SO_4 [35]	45	6	2	16	31	1.8	0.3
Passivation in D_2O with 0.05 M H_2SO_4	42	7	4	13	34	1.7	0.3

Table 1 Composition and thickness of the surface oxide films after immersion of the $Cr_{15}Fe_{10}Co_5Ni_{60}Mo_{10}$ surfaces in pure H_2O or D_2O, in acidified H_2O or D_2O, or anodic passivation in acidified H_2O or D_2O. Values were obtained from the XPS intensities using a bilayer model of intensity attenuation.

The composition and thickness of the oxide films obtained for surfaces prepared following the same procedure with or without deuteration reveal that the deuteration of the electrolyte did not lead to any significant modifications in the composition nor thickness.

The structural consistency (supported by the depth profiles in Figure 3) and the compositional consistency (proven by Figure 2 and Table 1) between the non-

deuterated and deuterated surfaces suggest that the use of D_2O in place of H_2O does not induce significant modification of the passivation mechanism and kinetics, possibly due to the extremely small depth dimension of the passivation reaction. The usability of non-deuterated surfaces as a reference for extracting D-containing signals is thus justified.

Regarding surface composition after different preparation procedures, comparison between the native oxide film and the oxide film after immersion in pure H_2O or D_2O reveals that the immersion in water led to slight thickening and Cr enrichment of the oxide film, with a decrease in Ni content. The decrease in Ni content and the increase in Cr content can be explained by the solubility of $Ni(OH)_2$ in water (0.0015 g/L)[58] and the stability of Cr hydroxide according to the Pourbaix diagram. However, after immersion in acid for the same duration, the Cr enrichment was less pronounced, while Mo species were further enriched. The impediment to Cr enrichment may be related to the dissolution of Cr hydroxide in acidic media. Both the decrease in equivalent oxide film thickness in Table 1 and the interface position at earlier sputtering times in Figure 3(c and d) also confirm that dissolution occurred to the oxide film during immersion in acid solution, which has been reported for stainless steels[21,59] and CrFeCoNi(Mn)(RuW) MPEAs[60,61]. The Mo enrichment caused by immersion at OCP has also been observed for NiCrFeRuMoW MPEA[60], which may be related to the difference in stability of Mo oxides in acid compared to other oxides. Regarding anodic passivation, evident thickening of the outer oxide layer was observed, accompanied by pronounced Cr and Mo enrichments and Ni depletion. These

observations substantiate that the electrochemical polarization in the passive range enhances the oxide film by promoting the Cr and Mo enrichments and the Ni dissolution[12,14,21,25,59–65].

3.3 Deuterated signals distribution

After verifying the oxide film consistency in the absence or presence of deuterium in the solution, the MO_xD^- (M = Cr, Ni, ^{100}Mo, Fe) signals were calculated using equation (1) in Section 2.3 for the three $Cr_{15}Fe_{10}Co_5Ni_{60}Mo_{10}$ surfaces treated in deuterated environment.

Figure 4 presents the depth profiles of the D^-, OD^-, and MO_xD^- signals normalized to bulk Ni_2^- intensity obtained for the three surfaces. As explained above, the D^- and OD^- signals reflect the general distribution of D atoms and OD hydroxyl groups, respectively. The CrO_3D^-, NiO_2D^-, and $^{100}MoO_3D^-$ signals represent deuterated Cr hydroxide, deuterated Ni hydroxide and deuterated Mo hydroxide, respectively. The overlap in mass between FeH_2^- (57.9506 amu) and Ni^- (57.9353 amu), and the low Fe content in the oxide[35] made the extracted deuterated Fe signal too noisy to develop reliable discussion. Therefore, the in-depth distribution of deuterated Fe hydroxides will not be discussed. The dashed lines mark the positions of the outer/inner oxide layer interfaces and oxide/alloy interfaces defined in Figure 3(b), (d), and (f). The fluctuations of the thus normalized intensities obtained during repetitive measurements performed at different locations on the same sample were less than 8 %.

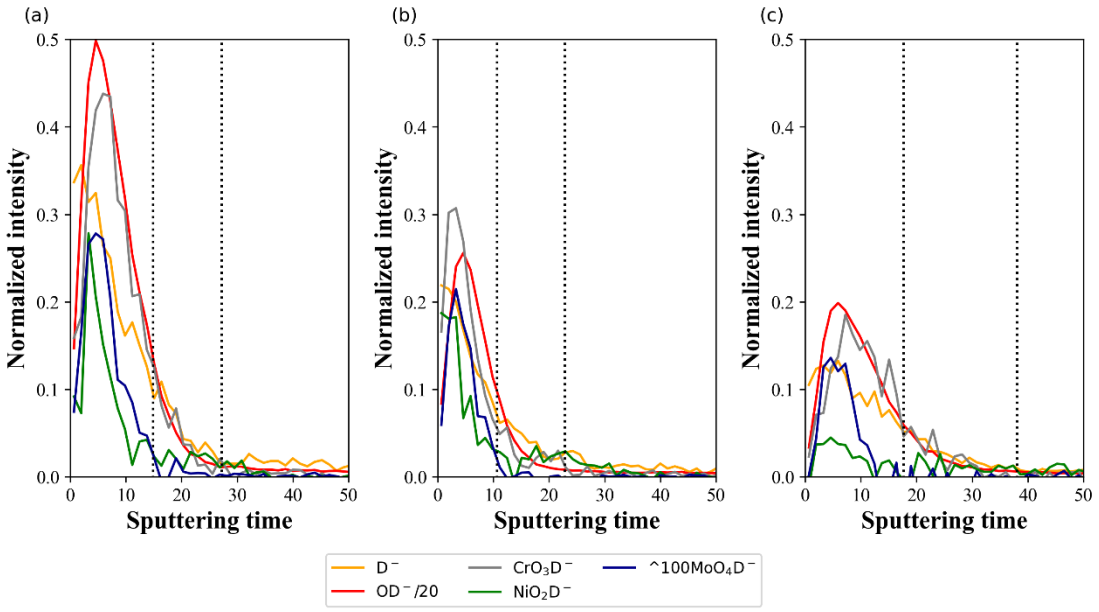

Figure 4 ToF-SIMS negative ion depth profiles of the deuterated signals for the $Cr_{15}Fe_{10}Co_5Ni_{60}Mo_{10}$ surface immersed at OCP in D_2O (a), in 0.05 M H_2SO_4 prepared with D_2O (b), or passivated at 0 V_{MSE} in 0.05 M H_2SO_4 prepared with D_2O (c).

For the $Cr_{15}Fe_{10}Co_5Ni_{60}Mo_{10}$ surface immersed in pure D_2O for 1 h 15 min (Figure 4(a)), all deuterated representative signals peak in the outer oxide layer region before reaching the inner/outer oxide interface. However, slight differences can be noticed in the sputtering time corresponding to their maximum intensity values. Among the general signals D^- and OD^-, the D^- signal peaks at earlier sputtering time than the OD^- signal. Among metal hydroxide signals, the NiO_2D^- signal peaks earlier than CrO_3D^- and $^{100}MoO_4D^-$ signals.

These depth profiles indicate that there is deuterium in the oxide film even after immersion in pure D_2O, and that the deuterated species concentrate principally in the outer oxide layer. Previous works on Cr oxide [66,67] and Fe oxides[68] suggest that pure water in gaseous or liquid state can interact with metal oxides via dissociative chemisorption[67–69]. On the oxide surface, water molecules dissociate into OH and

H, followed by OH adsorption on metal cations via cation-O bonding and H adsorption on oxygen anions initially forming the oxide surface. The dissociative chemisorption of water molecules could be one reason for having deuterated species in the oxide film. Besides, considering the D and H concentration gradient between the water and the oxide film, the H/D isotopic exchange[70,71] cannot be ignored, which could be another important reason for having deuterium into the outer oxide layer.

The maximal intensity of the D^- signal observed at the very beginning of sputtering, earlier than for OD^-, suggests that globally the preferential location of D atoms is more superficial than that of O, making OD fragments sputtered out later than D alone. This superficial distribution of D may indicate the existence of some protruding D terminations on the oxide surface[68].

Regarding the deuterated metal hydroxides characterized by CrO_3D^-, NiO_2D^- and $^{100}MoO_4D^-$, the difference in sputtering times for reaching their maximum intensity indicates that deuterated Ni hydroxide is more superficial than deuterated Cr and Mo hydroxides. This fine stratification exists also between normal Ni, Cr, and Mo species in non-deuterated oxide film as shown in Figure 3, meaning that the deuterated hydroxides followed the same distribution as the non-deuterated species of corresponding elements in the outer oxide layer.

Figure 4(b) shows the depth profiles of deuterated species for the $Cr_{15}Fe_{10}Co_5Ni_{60}Mo_{10}$ surface immersed at OCP in acidified D_2O. Again, the peaks of the deuterated signals are all located in the outer oxide layer region, and the D^- ion profile peaks earlier than that of OD^-. The difference in peak locations of the NiO_2D^-,

CrO_3D^-, and $^{100}MoO_4D^-$ signals decreases. It is noteworthy that the relative location of the OD^- peak in the outer layer becomes slightly deeper in Figure 4(b), whereas it was relatively more superficial in Figure 4(a). Besides, the intensities of all D-containing signals in Figure 4(b) are lower than in Figure 4(a).

The profiles in Figure 4(b) confirm the existence of deuterated species in the outer oxide layer of the surface oxide film after immersion at OCP in acidified deuterated water. The more superficial distribution of D than O is retained as supported by the respective location of the D^- and OD^- peaks, whereas the stratification between deuterated Ni, Cr, Mo hydroxides became less evident, possibly due to thinning of the oxide film as discussed above. Since the OD^- profile is determined by the contribution of various (oxy)hydroxides and adsorbed hydroxyl/water, its relative deeper location in the outer layer could result from enhanced dissolution of some hydroxylated components at extreme surface in the acidified solution[66,72]. Regarding the intensity decrease compared to neutral solution, it cannot be excluded that the compositional changes induced by dissolution resulted in ion yield changes. However, the lower intensity level measured for deuterated species agrees well with the proposition that dissolution of the surface hydroxides occurred when the water was acidified.

Figure 4(c) shows the depth profiles of D-containing components for the surface anodically passivated in acidified D_2O. Expectedly, the profiles of the deuterated species still peak in the outer oxide layer region. However, compared to Figure 4(b), the intensities of all deuterated signals further decrease, especially that of the NiO_2D^- signal. Broadening of the CrO_3D^- profile is observed, whereas it is not observed for

$^{100}MoO_4D^-$.

The location of the peaks in Figure 4(c) demonstrates that deuterated species also exist for the passive oxide film and are located principally in the outer layer. The relative peak positions of the $^{100}MoO_4D^-$ and CrO_3D^- signals indicate that the deuterated Mo species are distributed in the outer part of the outer layer of the passive film, while the deuterated Cr species are concentrated at a slightly deeper position in the outer oxide layer. The significantly lower intensity of NiO_2D^- signal is in agreement with the diminution of Ni content observed after anodic passivation (Table 1), indicating the preferential dissolution of Ni hydroxide induced by anodic electrochemical polarization in the passive range[13,35,60,63]. No evident intensity increase was observed for all these deuterated signals after anodic passivation compared to immersion at OCP in water or acid solution. Under the assumption that the ion sputtering yields were not markedly modified, it can be inferred that the re-growth of the oxide film induced by anodic passivation is not accompanied by a pronounced surface uptake of deuterium from the electrolyte.

3.4 Hydroxyl transport mechanisms during passivation

To further understand the intensity variations of the deuterated-related signals, the correlation between elemental content of the surface oxide film and corresponding ToF-SIMS signal intensities was investigated. Based on the exploration and comparison of the oxide film cationic composition obtained by XPS and the ToF-SIMS signal intensities measured for the same CrFeCoNiMo MPEA surfaces after different preparation [34], a linearity was observed between the XPS-measured content of Cr

hydroxide in the outer oxide layer and the maximum intensity of the ToF-SIMS signal representing Cr hydroxide in equivalent measurement conditions. Figure 5 compares the intensity variation tendency of ToF-SIMS depth profile for non-deuterated (CrO_3H^- and $CrO_3H_2^-$) and deuterated (CrO_3D^-) Cr hydroxides with the content of Cr hydroxide in the outer oxide layer obtained by XPS for the three $Cr_{15}Fe_{10}Co_5Ni_{60}Mo_{10}$ surfaces, in order to elucidate the different behavior of OH^- and OD^- upon OCP and anodic passivation.

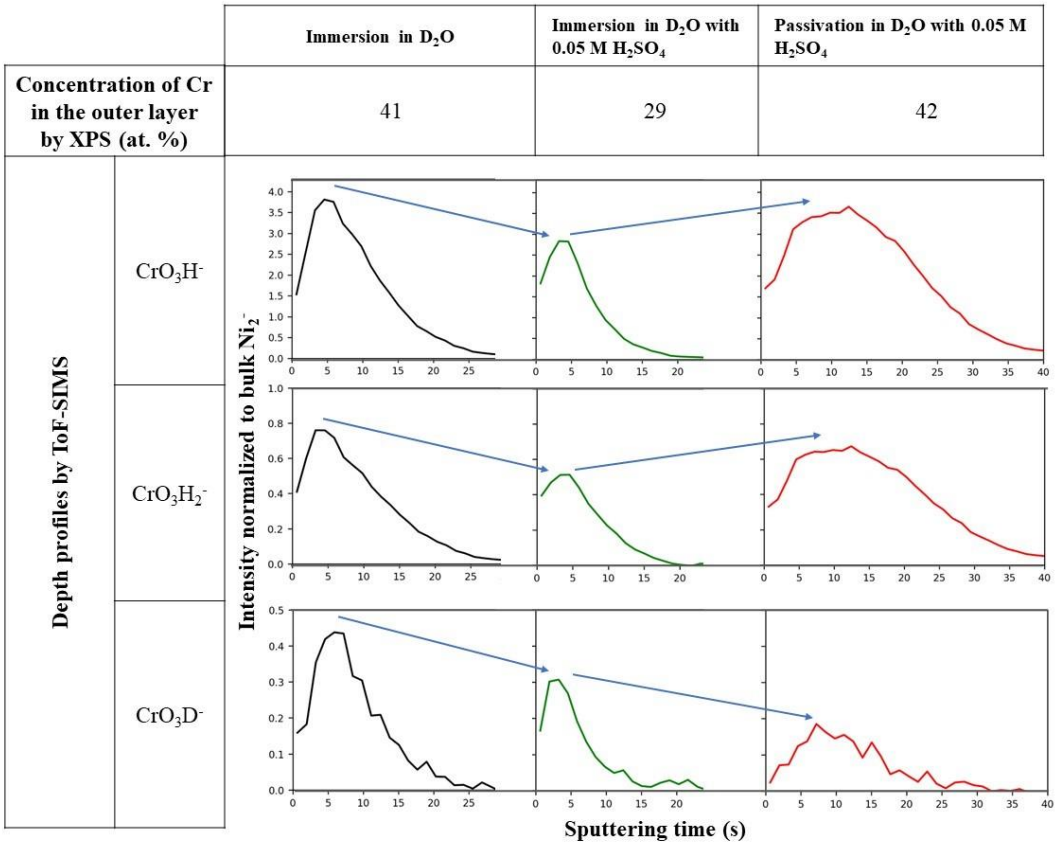

Figure 5 XPS-measured of Cr content in the outer oxide layer and ToF-SIMS depth profiles of representative ions for non-deuterated (CrO_3H^-, $CrO_3H_2^-$) and deuterated (CrO_3D^-) Cr hydroxide for $Cr_{15}Fe_{10}Co_5Ni_{60}Mo_{10}$ surfaces treated in three deuterated solutions.

Comparing the ToF-SIMS depth profiles after immersion at OCP in acidified D_2O to that in pure D_2O, the maximum intensity of all Cr characteristic signals CrO_3H^-,

$CrO_3H_2^-$, and CrO_3D^- decreased consistently with the Cr content in the outer layer measured by XPS. The ratio between maximal intensities $CrO_3D^-_{max}/CrO_3H_2^-_{max}$ was calculated to be 0.6 for both surfaces immersed at OCP. However, after anodic passivation, a divergence can be observed between non-deuterated and deuterated Cr hydroxide. Compared to immersion at OCP, the XPS-measured Cr content in the outer layer of passive oxide film increased to 42 at. %. The maximal intensity of CrO_3H^- and $CrO_3H_2^-$ increased correspondingly, whereas the maximal intensity of CrO_3D^- decreased. The maximum ratio $CrO_3D^-_{max}/CrO_3H_2^-_{max}$ was reduced to 0.3. This discrepancy demonstrates clearly that anodic passivation resulted in a higher proportion of non-deuterated Cr hydroxide among Cr hydroxide in the final passive film.

The only source of non-deuterated hydroxyl OH^- in these experiments was the OH^- coming from hydroxide species ($Ni(OH)_2$, $Fe(OH)_2$, and $Fe(OH)_3$) originally present in the native oxide film. Therefore, one may ask whether the higher non-deuterated Cr hydroxide proportion is due to the limitation of dissolution upon anodic passivation or related to the ion transport mechanism. Table 2 compiles the amounts of cations measured in the electrolyte by ICP-OES after passivation, and the amount of cations contained in the native and passive oxide films measured by XPS.

Cation	Cationic amount ($10^{-9}\ mol \cdot cm^{-2}$)		
	In electrolyte (by ICP-OES)	In the outer layer of the native oxide film (by XPS)	In the outer layer of the passive oxide film (by XPS)
Cr	$1.7(\pm 0.5)$	$0.9(\pm 0.1)$	$2.6(\pm 0.1)$
Fe	$4.1(\pm 0.7)$	$0.7(\pm 0.1)$	$0.5(\pm 0.1)$
Co	$1.1(\pm 0.2)$	$0.2(\pm 0.1)$	$0.2(\pm 0.1)$
Ni	$17.5(\pm 0.7)$	$2.5(\pm 0.1)$	$0.8(\pm 0.1)$
Mo	$1.8(\pm 0.4)$	$1.1(\pm 0.1)$	$2.1(\pm 0.1)$

Table 2 Quantity of cations contained in the electrolyte as measured by ICP-OES analysis after anodic passivation, and in the native and passive oxide films on $Cr_{15}Fe_{10}Co_5Ni_{60}Mo_{10}$ surfaces as obtained from XPS

analysis.

The amounts of cations in the electrolyte and in the oxide films confirm again the enhanced dissolution of Ni, Fe species and the enrichment of Cr, Mo species in oxide film induced by passivation. Besides, comparing the quantities of cations dissolved into the electrolyte to those contained in the oxide films, the quantity of dissolved cations was not of minor extent. Therefore, the higher non-deuterated Cr hydroxide proportion in the passive oxide film should be related to enhanced formation of non-deuterated Cr hydroxide and/or hindered formation of deuterated Cr hydroxide upon anodic passivation.

To form new non-deuterated Cr hydroxide in deuterated solution, OH^- could only come from the hydroxide species initially contained in the native oxide film, i.e., in Ni hydroxide, and possibly in Fe and Mo hydroxides if there were such species. Since less Ni and Fe are measured in the final passive oxide film, Ni and Fe hydroxides could be considered as suppliers of OH^-. Thus, it is reasonable to propose that under the electrical field applied for anodic passivation, the mobility of OH^- originating from Ni (and Fe) hydroxides is reduced. These OH^- are retained at the interface between electrolyte and oxide layer instead of being released into electrolyte congruently with the cations. These OH^- participate then in forming Cr hydroxide, thus reducing the OD uptake from the electrolyte. As a result, the proportion of non-deuterated Cr hydroxide increases in the passive oxide film.

To support this hypothesis and to estimate whether the OH^- initially present in the native oxide film were enough for forming all newly grown Cr hydroxide, a balance

calculation was performed for OH^-. For simplification, species were considered in the form of $Cr(OH)_3$, $Ni(OH)_2$, $Fe(OH)_2$, and $Fe(OH)_3$. It was also assumed that all OH^- in dissolved species can be utilized. Due to the difficulty in identifying Fe oxide and hydroxide, the estimation of OH^- quantity was given for two extreme cases: all Fe species were hydroxides, and all Fe species were oxides. Co species were neglected due to their low content. Mo species were not considered since Mo quantity increased and its chemical nature was still uncertain. The compositional difference between the native and passive oxide films gives that the maximum OH^- quantity that could be given by dissolved $Ni(OH)_2$, $Fe(OH)_2$, and $Fe(OH)_3$ were $3.5 \times 10^{-9}\ mol \cdot cm^{-2}$, $0.3 \times 10^{-9}\ mol \cdot cm^{-2}$, and $0.3 \times 10^{-9}\ mol \cdot cm^{-2}$, respectively. In the case of all Fe species being hydroxides, the formation of $Cr(OH)_3$ could thus re-use $4.1 \times 10^{-9}\ mol \cdot cm^{-2}$ OH^- at the most. However, the OH^- contained in newly formed $Cr(OH)_3$ was $5.2 \times 10^{-9}\ mol \cdot cm^{-2}$. Therefore, at least $1.1 \times 10^{-9}\ mol \cdot cm^{-2}$ OD^- should still be taken from the electrolyte, amounting to 14 % of the total hydroxyl quantity in Cr hydroxide. If all Fe species were oxides and could not provide OH^-, the OD^- uptake from the electrolyte among all hydroxyl in Cr hydroxide would be 22 %.

All the observations show that, for the $Cr_{15}Fe_{10}Co_5Ni_{60}Mo_{10}$ MPEA, anodic passivation in acid solution enhances the enrichment of Cr and Mo of the surface oxide film by preferentially dissolving Ni and Fe initially present in the native oxide film. They also indicate that, in this process, the hydroxyls initially contained in Ni (and Fe) hydroxides are retained by the electric field instead of being released congruently into the electrolyte. These retained OH^- participate into the formation of Cr hydroxide, with

a small additional part complemented by OD^- from the electrolyte. In the case of 1 h anodic passivation, Cr hydroxide formation uses mainly OH^- originating from the dissolved hydroxides, and OD^- surface uptake from the electrolyte for forming Cr hydroxide is only of minor extent. This hypothesis can be confirmed by the thermodynamic constant for chromium hydroxide precipitation ($Cr^{3+} + 3OH^- \rightarrow Cr(OH)_3$, $Ks(Cr(OH)_3)=10^{-30}$) indicating that the formation of $Cr(OH)_3$ via precipitation of dissolved Cr^{3+} species is not favoured. This observation corroborates the additional formation of $Cr(OH)_3$ in the outer layer by a conversion reaction in the solid state, retaining only the OH^- initially present in the hydroxide layer and releasing Ni^{2+} and $Fe^{2+/3+}$. From these observations, a mechanism of formation of the outer oxide layer during anodic passivation is presented on Figure 6.

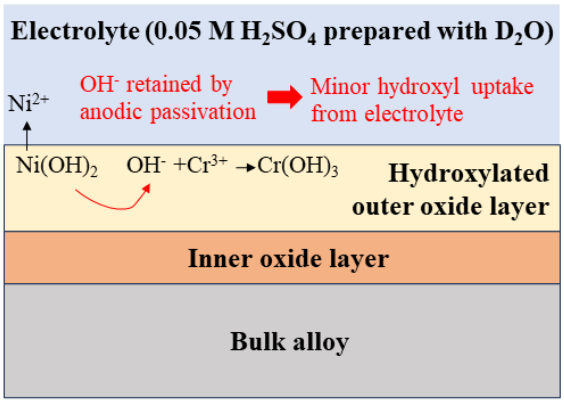

Figure 6: Mechanism of the outer oxide layer formation during anodic passivation in H_2SO_4 electrolyte prepared with D_2O.

Previous work has shown that, when passivated, $Cr_{15}Fe_{10}Co_5Ni_{60}Mo_{10}$ MPEA can sustain at least 4.7 M Cl^- without being corroded, whereas localized corrosion was already observed on SS 316L or Cantor alloys at 1 M or 0.3 M Cl^-, respectively [34].

The restrained hydroxyl uptake from the electrolyte may reflect a restrained anion uptake, which may contribute to the high corrosion resistance of the $Cr_{15}Fe_{10}Co_5Ni_{60}Mo_{10}$ alloy in chloride-containing medium [37]. In this previous work, it was clearly demonstrated that, for the same alloy, there is a limitation in the penetration of chloride anions into the outer layer during anodic passivation. In view of the results reported here, it seems established that there is competition between the formation of the new outer layer and the penetration of chlorides. Obviously, the action of the new outer layer alone is probably not sufficient to completely block the inward transport of anions towards the inner layer. Further work could investigate to which extent the penetration of chloride anions into the oxide film can be hindered by the abundance of reused hydroxyls.

Besides, ToF-SIMS depth profiling, both with or without isotopic labelling, evidences that there was almost no hydrogen in the inner layer of the surface oxide film. Hence, inwards OH^- diffusion until the alloy/oxide interface, which has been observed for oxide film growth in high temperature high pressure water[43,46], is excluded from being primary during the oxide film growth at room temperature (and standard atmosphere).

4 Conclusion

The hydroxyl transport mechanisms between electrolyte and outer part of the nanometer-thick passive oxide film on $Cr_{15}Fe_{10}Co_5Ni_{60}Mo_{10}$ MPEA surfaces in 0.05 M H_2SO_4 aqueous electrolyte were studied at room temperature and ambient pressure

using deuterium-labelled ToF-SIMS depth profiling, high-resolution XPS and ICP-OES.

The oxide film formed after immersion in pure water or sulfuric acid, or after anodic passivation in sulfuric acid retains the bilayer structure of the native oxide film. Thickness and composition of the oxide films show that although dissolution occurs during immersion in sulfuric acid, the oxide film is thickened with Cr and Mo enrichment during anodic passivation. Deuteration of the electrolyte has no effect on the passivation-induced alterations of the stratified structure and cationic composition of the nanometer-thick surface oxide film. A data treatment methodology for extracting the representative ToF-SIMS signals for deuterated species was developed, enabling the depth profile reconstruction for D-labelled species including deuterium atoms, deuterated hydroxyls, and deuterated Cr, Ni, Mo hydroxides. Surfaces immersed in pure or acidified D_2O exhibit deuterium uptake due to chemical interaction and isotopic exchange. The maximum intensities of the ToF-SIMS profiles for both deuterated and non-deuterated Cr hydroxides vary consistently with the content of Cr hydroxide in the outer layer measured by XPS. However, when being anodically passivated, the formation of non-deuterated Cr hydroxide is favored. Non-negligible extent of dissolution measured by ICP-OES and charge balance calculation suggested that the promoted formation of non-deuterated Cr hydroxide is related to the reutilization of hydroxyls initially in the native oxide film. It is thus suggested that during anodic passivation, the hydroxyls from the dissolving Ni (and Fe) hydroxides are retained by the electric field and form new Cr hydroxide, thus reducing the OD surface uptake from

the electrolyte.

CRediT authorship contribution statement

Xueying Wang: Investigation, Validation, Methodology, Visualization, Writing - Original Draft. **Dimitri Mercier:** Conceptualization, Validation, Methodology, Supervision, Writing - review & editing. **Sandrine Zanna:** Investigation, Data Curation. **Antoine Seyeux:** Investigation, Data Curation. **Loïc Perrière:** Resources. **Mathilde Laurent-Brocq:** Resources. **Ivan Guillot:** Resources. **Vincent Maurice:** Funding acquisition, Writing - review & editing. **Philippe Marcus:** Funding acquisition, Project management, Conceptualization, Supervision, Writing - review & editing.

Competing Interests

The authors declare that they have no known competing financial interests or personal relationships that could have appeared to influence the work reported in this paper.

Acknowledgments

This work was supported by the European Research Council (ERC) under the European Union's Horizon 2020 research and innovation programme (ERC Advanced Grant agreement No. 741123).

References

[1] J. Steffen, S. Hofmann, Oxidation of NiCr and NiCrFe alloys at room temperature, Surf. Interface Anal. 11 (1988) 617–626. https://doi.org/10.1002/sia.740111207.

[2] L. Ma, F. Wiame, V. Maurice, P. Marcus, Origin of nanoscale heterogeneity in the surface oxide film protecting stainless steel against corrosion, Npj Mater Degrad 3 (2019) 1–9. https://doi.org/10.1038/s41529-019-0091-4.

[3] H.H. Uhlig, Passivity in metals and alloys, Corros. Sci. 19 (1979) 777–791. https://doi.org/10.1016/S0010-938X(79)80075-X.

[4] H.-H. Strehblow, V. Maurice, P. Marcus, Passivity of Metals, in: P. Marcus (Ed.), Corrosion Mechanisms in Theory and Practice, 3rd Ed., 3rd ed., CRC Press, Taylor and Francis, 2011: pp. 235–326.

[5] M. Långberg, C. Örnek, J. Evertsson, G.S. Harlow, W. Linpé, L. Rullik, F. Carlà, R. Felici, E. Bettini, U. Kivisäkk, E. Lundgren, J. Pan, Redefining passivity breakdown of super duplex stainless steel by electrochemical operando synchrotron near surface X-ray analyses, NPJ Mater. Degrad. 3 (2019) 1–11. https://doi.org/10.1038/s41529-019-0084-3.

[6] N. Cabrera, N.F. Mott, Theory of the Oxidation of Metals, Rep. Prog. Phys. 12 (1949) 163. https://doi.org/10.1088/0034-4885/12/1/308.

[7] F.P. Fehlner, N.F. Mott, Low-temperature oxidation, Oxidation of Metals 2 (1970) 59–99.

[8] C.Y. Chao, L.F. Lin, D.D. Macdonald, A Point Defect Model for Anodic Passive Films: I . Film Growth Kinetics, J. Electrochem. Soc. 128 (1981) 1187. https://doi.org/10.1149/1.2127591.

[9] A. Seyeux, V. Maurice, P. Marcus, Oxide Film Growth Kinetics on Metals and Alloys: I. Physical Model, J. Electrochem. Soc. 160 (2013) C189–C196. https://doi.org/10.1149/2.036306jes.

[10] K. Leistner, C. Toulemonde, B. Diawara, A. Seyeux, P. Marcus, Oxide Film Growth Kinetics on Metals and Alloys: II. Numerical Simulation of Transient Behavior, J. Electrochem. Soc. 160 (2013) C197–C205. https://doi.org/10.1149/2.037306jes.

[11] C.-O.A. Olsson, S.E. Hörnström, An AES and XPS study of the high alloy austenitic stainless steel 254 SMO® tested in a ferric chloride solution, Corrosion Science 36 (1994) 141–151. https://doi.org/10.1016/0010-938X(94)90115-5.

[12] P. Marcus, I. Olefjord, A Round Robin on combined electrochemical and AES/ESCA characterization of the passive films on Fe-Cr and Fe-Cr-Mo alloys, Corros. Sci. 28 (1988) 589–602. https://doi.org/10.1016/0010-938X(88)90026-1.

[13] Z. Wang, C. Carrière, A. Seyeux, S. Zanna, D. Mercier, P. Marcus, XPS and ToF-SIMS Investigation of Native Oxides and Passive Films Formed on Nickel Alloys Containing Chromium and Molybdenum, J. Electrochem. Soc. 168 (2021) 041503. https://doi.org/10.1149/1945-7111/abf308.

[14] X. Zhang, D. Zagidulin, D.W. Shoesmith, Characterization of film properties on

the Ni-Cr-Mo Alloy C-2000, Electrochim. Acta 89 (2013) 814–822. https://doi.org/10.1016/j.electacta.2012.11.029.

[15] V. Maurice, W.P. Yang, P. Marcus, XPS and STM Study of Passive Films Formed on Fe-22Cr(110) Single-Crystal Surfaces, J. Electrochem. Soc. 143 (1996) 1182–1200. https://doi.org/10.1149/1.1836616.

[16] M.P. Ryan, R.C. Newman, G.E. Thompson, Atomically Resolved STM of Oxide Film Structures on Fe-Cr Alloys during Passivation in Sulfuric Acid Solution, J. Electrochem. Soc. 141 (1994) L164. https://doi.org/10.1149/1.2059380.

[17] M.P. Ryan, R.C. Newman, G.E. Thompson, A scanning tunnelling microscopy study of structure and structural relaxation in passive oxide films on Fe-Cr alloys, Philosophical Magazine B 70 (1994) 241–251. https://doi.org/10.1080/01418639408241803.

[18] D. Zuili, V. Maurice, P. Marcus, In situ Scanning Tunneling Microscopy Study of the Structure of the Hydroxylated Anodic Oxide Film Formed on Cr(110) Single-Crystal Surfaces, J. Phys. Chem. B 103 (1999) 7896–7905. https://doi.org/10.1021/jp9911088.

[19] L. Luo, L. Zou, D.K. Schreiber, M.J. Olszta, D.R. Baer, S.M. Bruemmer, G. Zhou, C.-M. Wang, In situ atomic scale visualization of surface kinetics driven dynamics of oxide growth on a Ni–Cr surface, Chem. Commun. 52 (2016) 3300–3303. https://doi.org/10.1039/C5CC09165A.

[20] B. Zhang, J. Wang, B. Wu, X.W. Guo, Y.J. Wang, D. Chen, Y.C. Zhang, K. Du, E.E. Oguzie, X.L. Ma, Unmasking chloride attack on the passive film of metals, Nat Commun 9 (2018) 2559. https://doi.org/10.1038/s41467-018-04942-x.

[21] B. Lynch, Z. Wang, L. Ma, E.-M. Paschalidou, F. Wiame, V. Maurice, P. Marcus, Passivation-Induced Cr and Mo Enrichments of 316L Stainless Steel Surfaces and Effects of Controlled Pre-Oxidation, J. Electrochem. Soc. 167 (2020) 141509. https://doi.org/10.1149/1945-7111/abc727.

[22] P. Marcus, J.M. Grimal, The anodic dissolution and passivation of NiCrFe alloys studied by ESCA, Corros. Sci. 33 (1992) 805–814. https://doi.org/10.1016/0010-938X(92)90113-H.

[23] I. Olefjord, B. Brox, U. Jelvestam, Surface composition of stainless steels during anodic dissolution and passivation studied by ESCA, J. Electrochem. Soc. 132 (1985) 2854–2861. https://doi.org/10.1149/1.2113683.

[24] A.S. Lim, A. Atrens, ESCA studies of Ni-Cr alloys, Appl. Phys. A 54 (1992) 343–349. https://doi.org/10.1007/BF00324199.

[25] V. Maurice, H. Peng, L.H. Klein, A. Seyeux, S. Zanna, P. Marcus, Effects of molybdenum on the composition and nanoscale morphology of passivated austenitic stainless steel surfaces, Faraday Discuss. 180 (2015) 151–170. https://doi.org/10.1039/C4FD00231H.

[26] T. Massoud, V. Maurice, L.H. Klein, P. Marcus, Nanoscale Morphology and Atomic Structure of Passive Films on Stainless Steel, J. Electrochem. Soc. 160 (2013) C232. https://doi.org/10.1149/2.067306jes.

[27] Z. Wang, E.-M. Paschalidou, A. Seyeux, S. Zanna, V. Maurice, P. Marcus, Mechanisms of Cr and Mo Enrichments in the Passive Oxide Film on 316L

Austenitic Stainless Steel, Front. Mater. 6 (2019) 232. https://doi.org/10.3389/fmats.2019.00232.

[28] P.-K. Huang, J.-W. Yeh, T.-T. Shun, S.-K. Chen, Multi-Principal-Element Alloys with Improved Oxidation and Wear Resistance for Thermal Spray Coating, Adv. Eng. Mater. 6 (2004) 74–78. https://doi.org/10.1002/adem.200300507.

[29] J.-W. Yeh, S.-K. Chen, S.-J. Lin, J.-Y. Gan, T.-S. Chin, T.-T. Shun, C.-H. Tsau, S.-Y. Chang, Nanostructured High-Entropy Alloys with Multiple Principal Elements: Novel Alloy Design Concepts and Outcomes, Adv. Eng. Mater. 6 (2004) 299–303. https://doi.org/10.1002/adem.200300567.

[30] C. Dai, T. Zhao, C. Du, Z. Liu, D. Zhang, Effect of molybdenum content on the microstructure and corrosion behavior of $FeCoCrNiMo_x$ high-entropy alloys, J. Mater. Sci. Technol. 46 (2020) 64–73. https://doi.org/10.1016/j.jmst.2019.10.020.

[31] X.-L. Shang, Z.-J. Wang, Q.-F. Wu, J.-C. Wang, J.-J. Li, J.-K. Yu, Effect of Mo Addition on Corrosion Behavior of High-Entropy Alloys $CoCrFeNiMo_x$ in Aqueous Environments, Acta Metall. Sin. (Engl. Lett.) 32 (2019) 41–51. https://doi.org/10.1007/s40195-018-0812-7.

[32] A.A. Rodriguez, J.H. Tylczak, M.C. Gao, P.D. Jablonski, M. Detrois, M. Ziomek-Moroz, J.A. Hawk, Effect of Molybdenum on the Corrosion Behavior of High-Entropy Alloys $CoCrFeNi_2$ and $CoCrFeNi_2Mo_{0.25}$ under Sodium Chloride Aqueous Conditions, Adv. Mater. Sci. Eng. 2018 (2018) 1–11. https://doi.org/10.1155/2018/3016304.

[33] Z. Niu, Y. Wang, C. Geng, J. Xu, Y. Wang, Microstructural evolution, mechanical and corrosion behaviors of as-annealed $CoCrFeNiMo_x$ (x = 0, 0.2, 0.5, 0.8, 1) high entropy alloys, J. Alloys Compd. 820 (2020) 153273. https://doi.org/10.1016/j.jallcom.2019.153273.

[34] X. Wang, D. Mercier, Y. Danard, T. Rieger, L. Perrière, M. Laurent-Brocq, I. Guillot, V. Maurice, P. Marcus, Enhanced passivity of Cr-Fe-Co-Ni-Mo multi-component single-phase face-centred cubic alloys: design, production and corrosion behaviour, Corros. Sci. 200 (2022) 110233. https://doi.org/10.1016/j.corsci.2022.110233.

[35] X. Wang, D. Mercier, S. Zanna, A. Seyeux, L. Perriere, M. Laurent-Brocq, I. Guillot, V. Maurice, P. Marcus, Origin of enhanced passivity of Cr–Fe–Co–Ni–Mo multi-principal element alloy surfaces, Npj Mater Degrad 7 (2023) 1–10. https://doi.org/10.1038/s41529-023-00330-z.

[36] C. Dai, H. Luo, J. Li, C. Du, Z. Liu, J. Yao, X-ray photoelectron spectroscopy and electrochemical investigation of the passive behavior of high-entropy FeCoCrNiMox alloys in sulfuric acid, Appl. Surf. Sci. 499 (2020) 143903. https://doi.org/10.1016/j.apsusc.2019.143903.

[37] X. Wang, D. Mercier, S. Zanna, A. Seyeux, L. Perriere, M. Laurent-Brocq, I. Guillot, V. Maurice, P. Marcus, Effects of Chloride Ions on Passive Oxide Films Formed on Cr-Fe-Co-Ni(-Mo) Multi-Principal Element Alloy Surfaces, J. Electrochem. Soc. 170 (2023) 041506. https://doi.org/10.1149/1945-7111/accb10.

[38] X. Huang, D. Costa, B. Diawara, V. Maurice, P. Marcus, Atomistic insights on enhanced passivity: DFT study of substitutional Mo on Cr2O3 and Fe2O3 surfaces,

Corrosion Science 224 (2023) 111543. https://doi.org/10.1016/j.corsci.2023.111543.

[39] A. Seyeux, Z. Wang, S. Zanna, C. Carrière, D. Mercier, P. Marcus, ToF-SIMS investigation with 18O isotopic tracer of the ion transport mechanisms in surface oxides on nickel-chromium and nickel-chromium-molybdenum alloys., Electrochimica Acta (2022) 140797. https://doi.org/10.1016/j.electacta.2022.140797.

[40] L. Wang, A. Seyeux, L. Perriere, D. Mercier, V. Maurice, P. Marcus, Insight on passivity of high entropy alloys: Thermal stability and ion transport mechanisms in the passive oxide film on CoCrFeMnNi surfaces, Corros. Sci. 188 (2021) 109540. https://doi.org/10.1016/j.corsci.2021.109540.

[41] C. Poulain, A. Seyeux, S. Voyshnis, P. Marcus, Volatilization and Transport Mechanisms During Cr Oxidation at 300 °C Studied In Situ by ToF-SIMS, Oxid Met 88 (2017) 423–433. https://doi.org/10.1007/s11085-017-9756-y.

[42] S. Voyshnis, A. Seyeux, S. Zanna, B. Martin-Cabanas, T. Couvant, P. Marcus, Oxide layer growth on nickel-base alloy surfaces in high temperature water and in O2 studied by ToF-SIMS with isotopic tracers, Corrosion Science 145 (2018) 212–219. https://doi.org/10.1016/j.corsci.2018.10.009.

[43] F. Jambon, L. Marchetti, F. Jomard, J. Chêne, Mechanism of hydrogen absorption during the exposure of alloy 600-like single-crystals to PWR primary simulated media, Journal of Nuclear Materials 414 (2011) 386–392. https://doi.org/10.1016/j.jnucmat.2011.04.066.

[44] T. Terachi, K. Fujii, K. Arioka, Microstructural Characterization of SCC Crack Tip and Oxide Film for SUS 316 Stainless Steel in Simulated PWR Primary Water at 320°C, Journal of Nuclear Science and Technology 42 (2005) 225–232. https://doi.org/10.1080/18811248.2005.9726383.

[45] A.N. Itakura, N. Miyauchi, Y. Murase, T. Yakabe, M. Kitajima, S. Aoyagi, Model of local hydrogen permeability in stainless steel with two coexisting structures, Sci Rep 11 (2021) 8553. https://doi.org/10.1038/s41598-021-87727-5.

[46] Z. Wang, Y. Takeda, Mechanistic understanding of the roles of hydrogen in modification of oxide film of alloy 600 in high temperature high pressure water environment, Corrosion Science 170 (2020) 108656. https://doi.org/10.1016/j.corsci.2020.108656.

[47] X. Wu, A. Seyeux, I. Vickridge, S. Voyshnis, P. Marcus, ToF-SIMS and ERDA study of hydrogen and deuterium in nickel-base alloys oxidized in water, Corrosion Science 140 (2018) 151–158. https://doi.org/10.1016/j.corsci.2018.06.006.

[48] C.D. Beachem, A new model for hydrogen-assisted cracking (hydrogen “embrittlement”), Metall Trans 3 (1972) 441–455. https://doi.org/10.1007/BF02642048.

[49] Z. Zhang, K.L. Moore, G. McMahon, R. Morana, M. Preuss, On the role of precipitates in hydrogen trapping and hydrogen embrittlement of a nickel-based superalloy, Corrosion Science 146 (2019) 58–69. https://doi.org/10.1016/j.corsci.2018.10.019.

[50] F. Jambon, L. Marchetti, F. Jomard, J. Chêne, Characterisation of oxygen and hydrogen migration through oxide scales formed on nickel-base alloys in PWR primary medium conditions, Solid State Ionics 231 (2013) 69–73. https://doi.org/10.1016/j.ssi.2012.10.012.

[51] X. Wang, D. Mercier, S. Zanna, A. Seyeux, L. Perriere, M. Laurent-Brocq, I. Guillot, V. Maurice, P. Marcus, XPS study of the thermal stability of passivated NiCrFeCoMo multi-principal element alloy surfaces, Surf. Interface Anal. 55 (2023) 457–465. https://doi.org/10.1002/sia.7193.

[52] X. Liu, T.S. Bjørheim, L. Vines, Ø.S. Fjellvåg, C. Granerød, Ø. Prytz, T. Yamamoto, H. Kageyama, T. Norby, R. Haugsrud, Highly Correlated Hydride Ion Tracer Diffusion in SrTiO3–xHx Oxyhydrides, J. Am. Chem. Soc. 141 (2019) 4653–4659. https://doi.org/10.1021/jacs.8b12985.

[53] D.R. Cole, S. Chakraborty, Rates and Mechanisms of Isotopic Exchange, Reviews in Mineralogy and Geochemistry 43 (2001) 83–223. https://doi.org/10.2138/gsrmg.43.1.83.

[54] H.C. Urey, Some Thermodynamic Properties of Hydrogen and Deuterium. Les Prix Nobel en 1934. 1st Edition. Stockholm: Kungl. Boktryckeriet P. A. Norstedt & Söner, 1935., Kungl. Boktryckeriet P. A. Norstedt & Söner, Stockholm, 1935.

[55] T. Jabs, P. Borthen, H.-H. Strehblow, X-Ray Photoelectron Spectroscopic Examinations of Electrochemically Formed Passive Layers on Ni-Cr Alloys, J. Electrochem. Soc. 144 (1997) 1231. https://doi.org/10.1149/1.1837577.

[56] J.H. Scofield, Hartree-Slater subshell photoionization cross-sections at 1254 and 1487 eV, J. Electron Spectrosc. Relat. Phenom. 8 (1976) 129–137. https://doi.org/10.1016/0368-2048(76)80015-1.

[57] S. Tanuma, C.J. Powell, D.R. Penn, Calculations of electron inelastic mean free paths. II. Data for 27 elements over the 50–2000 eV range, Surf. Interface Anal. 17 (1991) 911–926. https://doi.org/10.1002/sia.740171304.

[58] W.M. Haynes, D.R. Lide, T.J. Bruno, eds., CRC handbook of chemistry and physics, 95th ed., CRC Press, Taylor & Francis Group, 2014.

[59] L. Ma, E.-M. Pascalidou, F. Wiame, S. Zanna, V. Maurice, P. Marcus, Passivation mechanisms and pre-oxidation effects on model surfaces of FeCrNi austenitic stainless steel, Corrosion Science 167 (2020) 108483. https://doi.org/10.1016/j.corsci.2020.108483.

[60] X. Li, J. Han, P. Lu, J.E. Saal, G.B. Olson, G.S. Frankel, J.R. Scully, K. Ogle, Communication—Dissolution and Passivation of a Ni-Cr-Fe-Ru-Mo-W High Entropy Alloy by Elementally Resolved Electrochemistry, J. Electrochem. Soc. 167 (2020) 061505. https://doi.org/10.1149/1945-7111/ab7f86.

[61] J. Han, A.Y. Gerard, P. Lu, J.E. Saal, K. Ogle, J.R. Scully, Elementally Resolved Dissolution Kinetics of a Ni-Fe-Cr-Mn-Co Multi-Principal Element Alloy in Sulfuric Acid Using AESEC-EIS, J. Electrochem. Soc. 169 (2022) 081507. https://doi.org/10.1149/1945-7111/ac862b.

[62] K.F. Quiambao, S.J. McDonnell, D.K. Schreiber, A.Y. Gerard, K.M. Freedy, P. Lu, J.E. Saal, G.S. Frankel, J.R. Scully, Passivation of a corrosion resistant high entropy alloy in non-oxidizing sulfate solutions, Acta Mater. 164 (2019) 362–376.

https://doi.org/10.1016/j.actamat.2018.10.026.

[63] A.Y. Gerard, J. Han, S.J. McDonnell, K. Ogle, E.J. Kautz, D.K. Schreiber, P. Lu, J.E. Saal, G.S. Frankel, J.R. Scully, Aqueous passivation of multi-principal element alloy Ni38Fe20Cr22Mn10Co10: Unexpected high Cr enrichment within the passive film, Acta Materialia 198 (2020) 121–133. https://doi.org/10.1016/j.actamat.2020.07.024.

[64] Z. Wang, F. Di-Franco, A. Seyeux, S. Zanna, V. Maurice, P. Marcus, Passivation-Induced Physicochemical Alterations of the Native Surface Oxide Film on 316L Austenitic Stainless Steel, J. Electrochem. Soc. 166 (2019) C3376–C3388. https://doi.org/10.1149/2.0321911jes.

[65] D. Hamm, K. Ogle, C.-O.A. Olsson, S. Weber, D. Landolt, Passivation of Fe–Cr alloys studied with ICP-AES and EQCM, Corrosion Science 44 (2002) 1443–1456. https://doi.org/10.1016/S0010-938X(01)00147-0.

[66] L. Zhang, X. Xiong, Y. Yan, K. Gao, L. Qiao, Y. Su, Atomic modeling for the initial stage of chromium passivation, Int J Miner Metall Mater 26 (2019) 732–739. https://doi.org/10.1007/s12613-019-1803-z.

[67] V. Maurice, S. Cadot, P. Marcus, Hydroxylation of ultra-thin films of α-Cr2O3(0001) formed on Cr(110), Surface Science 471 (2001) 43–58. https://doi.org/10.1016/S0039-6028(00)00880-3.

[68] M. Sterrer, N. Nilius, S. Shaikhutdinov, M. Heyde, T. Schmidt, H.-J. Freund, Interaction of water with oxide thin film model systems, Journal of Materials Research 34 (2019) 360–378. https://doi.org/10.1557/jmr.2018.454.

[69] M.A. Blesa, A.D. Weisz, P.J. Morando, J.A. Salfity, G.E. Magaz, A.E. Regazzoni, The interaction of metal oxide surfaces with complexing agents dissolved in water, Coordination Chemistry Reviews 196 (2000) 31–63. https://doi.org/10.1016/S0010-8545(99)00005-3.

[70] M.C. DePonte, J.A. Wilke, D.T. Boyle, M.Z. Gillum, D.A. Schlosser, V.H. Lam, H. Kaleem, E.M. Maxwell, A.E. Baber, Low–temperature exchange of hydrogen and deuterium between molecular ethanol and water on Au(111), Surface Science 680 (2019) 1–5. https://doi.org/10.1016/j.susc.2018.10.001.

[71] J.J. Grabowski, C.H. DePuy, V.M. Bierbaum, Gas-phase hydrogen-deuterium exchange reactions of hydroxide and hydroxide-d ions with weakly acidic neutrals, J. Am. Chem. Soc. 105 (1983) 2565–2571. https://doi.org/10.1021/ja00347a009.

[72] L. Björnkvist, I. Olefjord, The electrochemistry of chromium in acidic chloride solutions: Anodic dissolution and passivation, Corrosion Science 32 (1991) 231–242. https://doi.org/10.1016/0010-938X(91)90045-Q.